JACS
JOURNAL OF THE AMERICAN CHEMICAL SOCIETY
pubs.acs.org/JACS

Open Access
This article is licensed under CC-BY-NC-ND 4.0

Article

# $MnSi_2Te_4$: A van der Waals Antiferromagnetic Semiconductor with Large Negative Magnetoresistance

Ke Liao,[¶] Bo Yin,[¶] Yue Pan,[¶] Long Chen,* Chen Liu, Yan Wu, Seung-Hwan Do, Yifan Gao, Yaling Yang, Yulong Wang, Xuhui Wang, Ying Li, Zhongnan Guo, Junwei Liu, Jiaou Wang, Dong Su, Jie Ma, Quansheng Wu,* and Gang Wang*

Cite This: J. Am. Chem. Soc. 2026, 148, 340−348

Read Online

ACCESS | Metrics & More | Article Recommendations | Supporting Information

**ABSTRACT:** Magnetism in van der Waals semiconductors offers significant potential for fundamental research on low-dimensional magnetism and the development of high-performance two-dimensional spintronic devices. Here, we report the growth, physical properties, and first-principles calculations of a new dual-octahedral transition metal chalcogenide (DTMC) $MnSi_2Te_4$. $MnSi_2Te_4$ features a layered structure with an intralayer heterostructure, where the metal octahedra and nonmetal dimeric octahedra form zigzag chains alternately. Property characterization reveals that $MnSi_2Te_4$ is a collinear G-type antiferromagnetic semiconductor, with a Néel temperature $T_N$ of 18.6 K and a significant unsaturated negative magnetoresistance (NMR) reaching −42.5% at 9 T and 100 K. First-principles calculations on the electronic band structure demonstrate that the large NMR primarily originates from the spin splitting due to parity-time symmetry breaking. This study not only discovers a new member of DTMCs with a unique crystal structure and large NMR, but also establishes a promising platform for investigating next-generation spintronic devices.

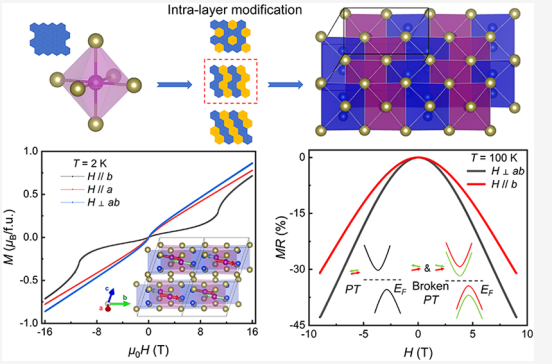


## INTRODUCTION

van der Waals (vdW) magnetic semiconductors have garnered considerable interest over the past decades owing to their peculiar properties and potential applications in electronic devices.[1,2] The combination of high tunability arising from the semiconductor nature and the long-range two-dimensional (2D) magnetism enables vdW magnetic semiconductors to regulate charge and spin simultaneously,[3,4] rendering them promising candidates for spintronic devices, including magnetic storage, spin-polarized carrier generation, spin filtering, and logic computation.[5−7] The 2D structure also facilitates the construction of vdW heterostructures, which can host novel interfacial transport properties with minimal lattice mismatch.[8] Moreover, some vdW magnetic semiconductors have exhibited tunneling magnetoresistance (MR) and large negative magnetoresistance (NMR), yielding enhanced performance in modern magnetic sensors.[9]

Transition metal octahedra, serving as the fundamental building blocks of transition metal chalcogenides (TMCs) with relatively weak interlayer coupling, allow for the construction of various types of intrinsic vdW magnetic semiconductors through interlayer or intralayer structural modifications (Figure 1).[10] Simple stacking of identical transition metal octahedra leads to transition metal dichalcogenides (TMDs),[11−13] while interlayer intercalation leads to the formation of intercalated TMDs.[14−16] Despite numerous theoretical predictions of potential vdW magnets from these two categories,[17−19] very few of them can be experimentally realized, and most of them exhibit metallic behavior.[20,21] Achieving the coexistence of intrinsic magnetism and semiconducting properties in vdW materials remains a significant challenge.[10,22] By the ordered substitution of nonmetal dimeric octahedra for metal octahedra, an emerging family of ternary transition metal chalcogenides can be obtained, namely, dual-octahedral transition metal chalcogenides (DTMCs). Notable examples of DTMCs include $MnPSe_3$,[23,24] $CrGeTe_3$,[25−27] and $CrSiTe_3$,[28,29] which demonstrate remarkable low-dimensional phenomena, such as intrinsic long-range magnetism in the 2D limit and positive/negative large magnetoresistance. Additionally, the intercalation of metal atoms into the interlayer space of DTMCs leads to other types of novel quasi-2D compounds, such as $Mn_3Si_2Te_6$,[30,31] which can be thought of as an example of interlayer structural modification. DTMCs typically exhibit a honeycomb-like intralayer arrangement of metal octahedra and nonmetal dimeric octahedra, naturally inspiring researchers to

Received: August 6, 2025
Revised: December 11, 2025
Accepted: December 15, 2025
Published: December 22, 2025

Downloaded via INST OF PHYSICS on January 20, 2026 at 01:36:53 (UTC).
See https://pubs.acs.org/sharingguidelines for options on how to legitimately share published articles.

© 2025 The Authors. Published by American Chemical Society

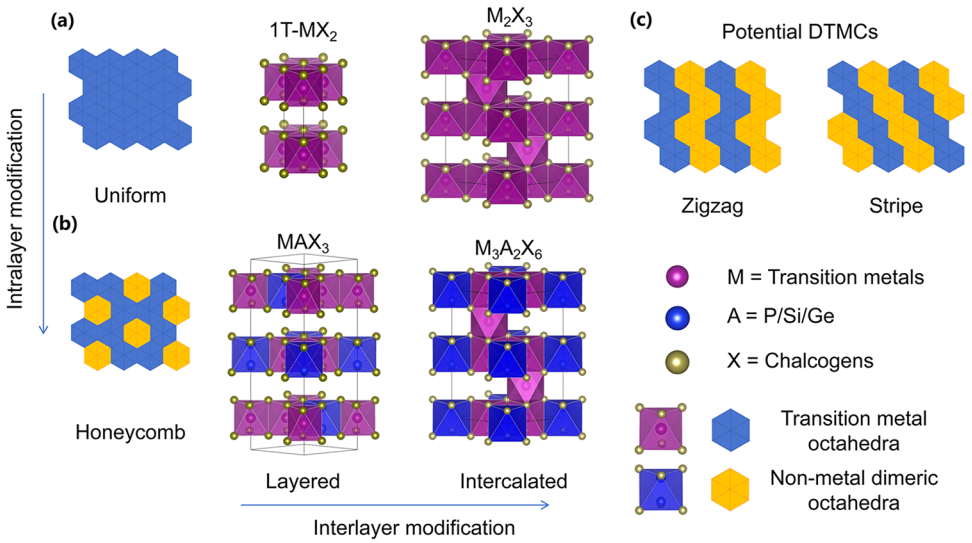


**Figure 1.** Designing new types of TMCs via interlayer or intralayer structural modifications. (a) Homogeneous octahedral arrangements in conventional TMDs (e.g., 1T-$MX_2$) or self-intercalated TMDs (e.g., $M_2X_3$). (b) Honeycomb octahedral arrangements in previously reported DTMCs (e.g., $MAX_3$) and intercalated DTMCs (e.g., $M_3A_2X_6$). (c) Other types of intralayer arrangements for octahedra in potential DTMCs.

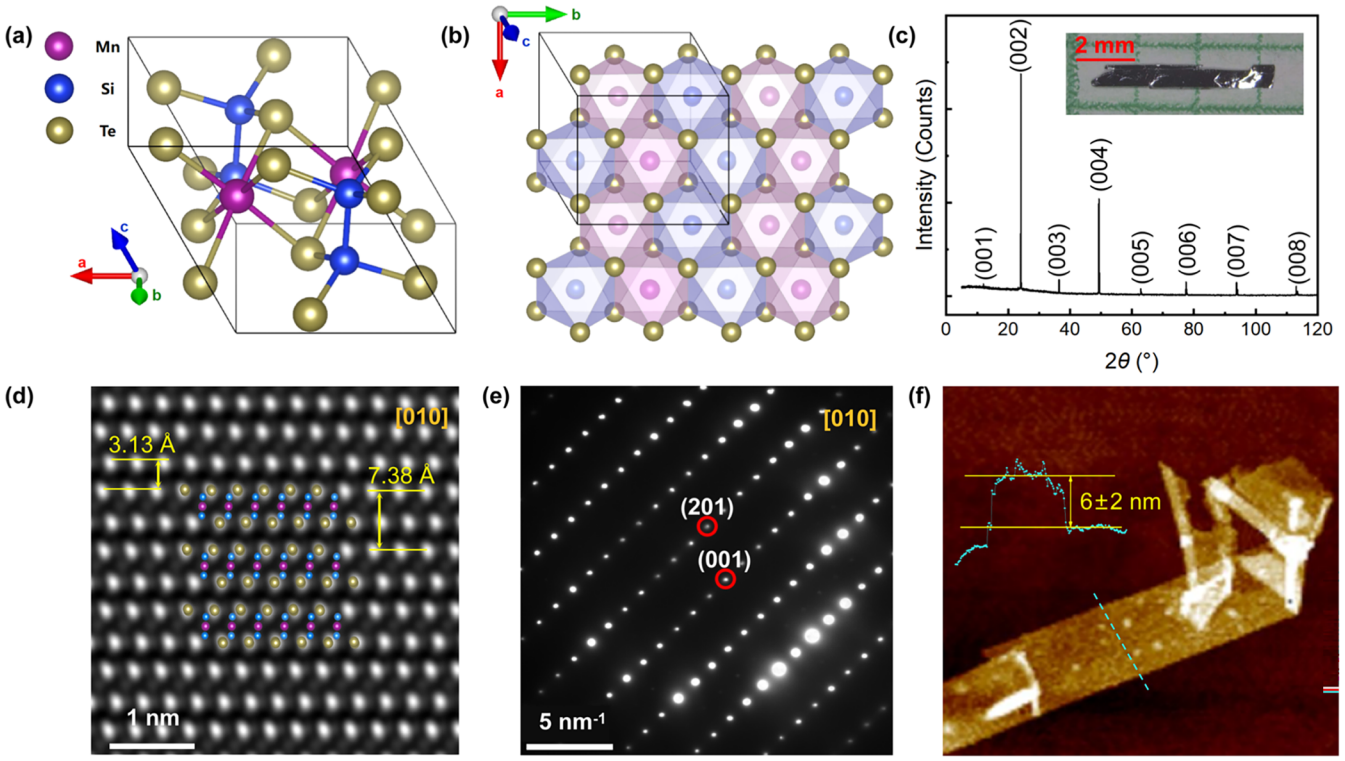


**Figure 2.** Intralayer heterostructure and vdW features of $MnSi_2Te_4$. (a) Crystal structure determined from SCXRD. (b) Schematic diagram of the zigzag arrangement of [$MnTe_6$] and [$Si_2Te_6$] octahedra. (c) XRD pattern of the $MnSi_2Te_4$ single crystal. The inset shows an optical image of a representative as-grown single crystal. (d) HAADF-STEM image of the $MnSi_2Te_4$ crystal acquired along the *b*-axis, illustrating the basal plane spacing and the interlayer distance. (e) SAED pattern of the $MnSi_2Te_4$ crystal acquired along the *b*-axis. (f) Atomic force microscopy image of the exfoliated $MnSi_2Te_4$ thin flake with the corresponding height profile.

explore the possibility of other intralayer arrangements, such as zigzag or stripe. However, stemming from the possible limitations imposed by synthesis conditions or structural stability, experimental reports on DTMCs with nonhoneycomb arrangements are still scarce. On the other hand, the experimental realization of nonhoneycomb intralayer arrangements will give more insight into the exploration of new vdW materials and corresponding functionalities.

Herein, we report the successful single-crystal synthesis and physical property characterization of a new Mn-based vdW antiferromagnetic (AFM) semiconductor, $MnSi_2Te_4$. The [$MnTe_6$] metal octahedra and [$Si_2Te_6$] nonmetal dimeric octahedra in $MnSi_2Te_4$ form zigzag chains alternately to construct an intralayer heterostructure, subsequently stacking into the three-dimensional DTMC structure with a moderate interlayer separation. Magnetic susceptibility, isothermal


https://doi.org/10.1021/jacs.5c13595
J. Am. Chem. Soc. 2026, 148, 340−348

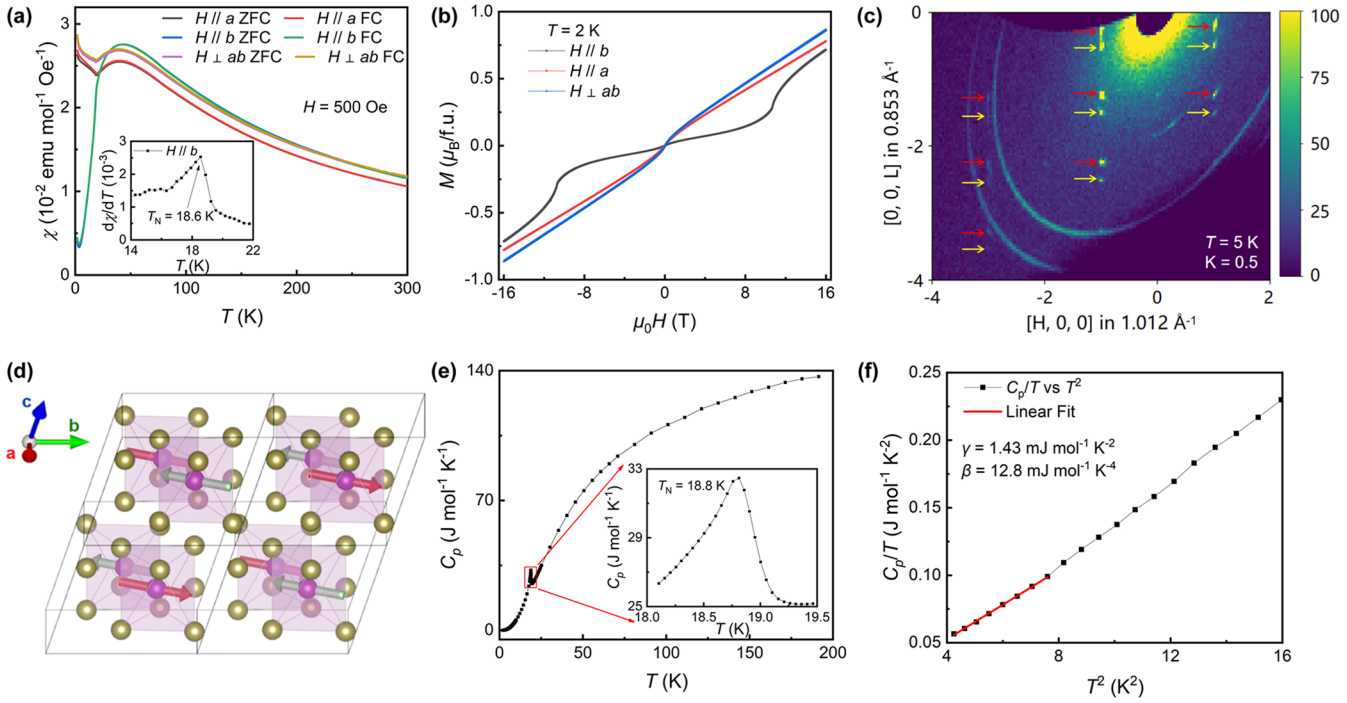


**Figure 3.** Uniaxial anisotropic AFM ground state. (a) Temperature-dependent magnetic susceptibility measured in ZFC and FC protocols under magnetic fields in different directions. The inset shows the $d\chi/dT$ vs $T$ plot along with the Néel temperature $T_N$ for $H \parallel b$. (b) Isothermal magnetization curves measured at 2 K under magnetic fields with different directions. (c) Single-crystal neutron diffraction pattern in the ($H$, 0.5, and $L$) scattering plane at 5 K, where the yellow and red arrows denote the magnetic peaks corresponding to magnetic wave vectors of $q_1$ = (0, −0.5, and 0.5) and $q_2$ = (0, 0.5, and −0.25), respectively. (d) Schematic diagram of the refined magnetic structure, with red and green arrows representing opposite magnetic moments. For clarity, only [$MnTe_6$] octahedra are displayed. (e) Temperature-dependent specific heat capacity. The inset shows a magnified view of specific heat capacity near the transition temperature. (f) $C_p/T$ vs $T^2$ plot in the low-temperature region with linear fitting based on the Debye model.

magnetization, and single-crystal neutron diffraction measurements collectively reveal a collinear G-type AFM ordering below $T_N$ = 18.6 K, with the easy axis aligned approximately along the $b$-axis. Specific heat capacity further confirms the AFM transition and hints at a semiconductive character with a nearly negligible Sommerfeld coefficient, which is confirmed by the temperature-dependent resistivity. The in-plane heterostructure also results in anisotropic in-plane resistivity and different magnitudes of angle-dependent MR with current applied along different directions. Moreover, a notable unsaturated NMR was observed with decreasing temperature, reaching −42.5% at 100 K under 9 T, where the spin splitting induced by the parity-time ($PT$) symmetry breaking under an external magnetic field serves as the primary mechanism of such a large NMR. $MnSi_2Te_4$ not only offers insights into designing new vdW magnetic semiconductors with unique crystal and magnetic structure, but also represents a versatile platform for exploring the fundamentals of 2D magnetism and developing novel spintronic devices.

## RESULTS AND DISCUSSION

**Crystal Structure.** Revealed by single-crystal X-ray diffraction (SCXRD), $MnSi_2Te_4$ crystallizes in a triclinic space group $P\bar{1}$ (No. 2) with lattice parameters $a$ = 6.8715(4) Å, $b$ = 8.0842(5) Å, $c$ = 8.3731(5) Å, $\alpha$ = 75.8555(17)°, $\beta$ = 66.2416(16)°, and $\gamma$ = 89.9983(16)° (Tables S1 and S2). As a member of DTMCs, $MnSi_2Te_4$ is composed of quintuple layers formed by the ordered arrangement of [$MnTe_6$] and [$Si_2Te_6$] octahedra, which stack along the crystallographic $c$-axis, forming a layered structure. In contrast to previously reported DTMCs featuring honeycomb lattices,[32−34] the transition metal octahedra [$MnTe_6$] and nonmetal dimeric octahedra [$Si_2Te_6$] in $MnSi_2Te_4$ are arranged in zigzag chains along the $a$-axis, alternating along the $b$-axis, resulting in an intralayer heterostructure (Figure 2a,b). Such variation in the arrangement of octahedra leads to a pronounced reduction of symmetry and enhanced octahedral distortion compared to honeycomb lattice counterparts (Figure S1 and Tables S3 and S4). The as-grown $MnSi_2Te_4$ single crystals appear as shiny, black stripe-like flakes, with the chemical composition Mn/Si/Te = 1:2:4 and $Mn^{2+}$ bonding state determined via energy-dispersive spectroscopy (EDS) and X-ray photoelectron spectroscopy (XPS), respectively (Figures S2 and S3). The X-ray diffraction (XRD) pattern of the crystal exclusively exhibits sharp (00$l$) ($l$ = integer) diffraction peaks, indicating that the crystal surface is parallel to the $ab$-plane. The interplanar spacing determined by the position of the (001) diffraction peak at 12.0° is 7.39 Å, consistent with the interlayer spacing $d$(00$l$) obtained from SCXRD (Figure 2c).

To investigate the intralayer and interlayer atomic arrangement, the $MnSi_2Te_4$ specimen was examined with high-angle annular dark-field scanning transmission electron microscopy (HAADF-STEM). The HAADF-STEM images and the selected-area electron diffraction (SAED) patterns (Figures 2d,e and S4) are in good agreement with the structure determined from SCXRD data, which clearly reveal the alternating arrangement of octahedral chains, further confirming the high crystalline quality of the $MnSi_2Te_4$ single crystal. The HAADF-STEM images also reveal the layered structure of


https://doi.org/10.1021/jacs.5c13595
J. Am. Chem. Soc. 2026, 148, 340−348

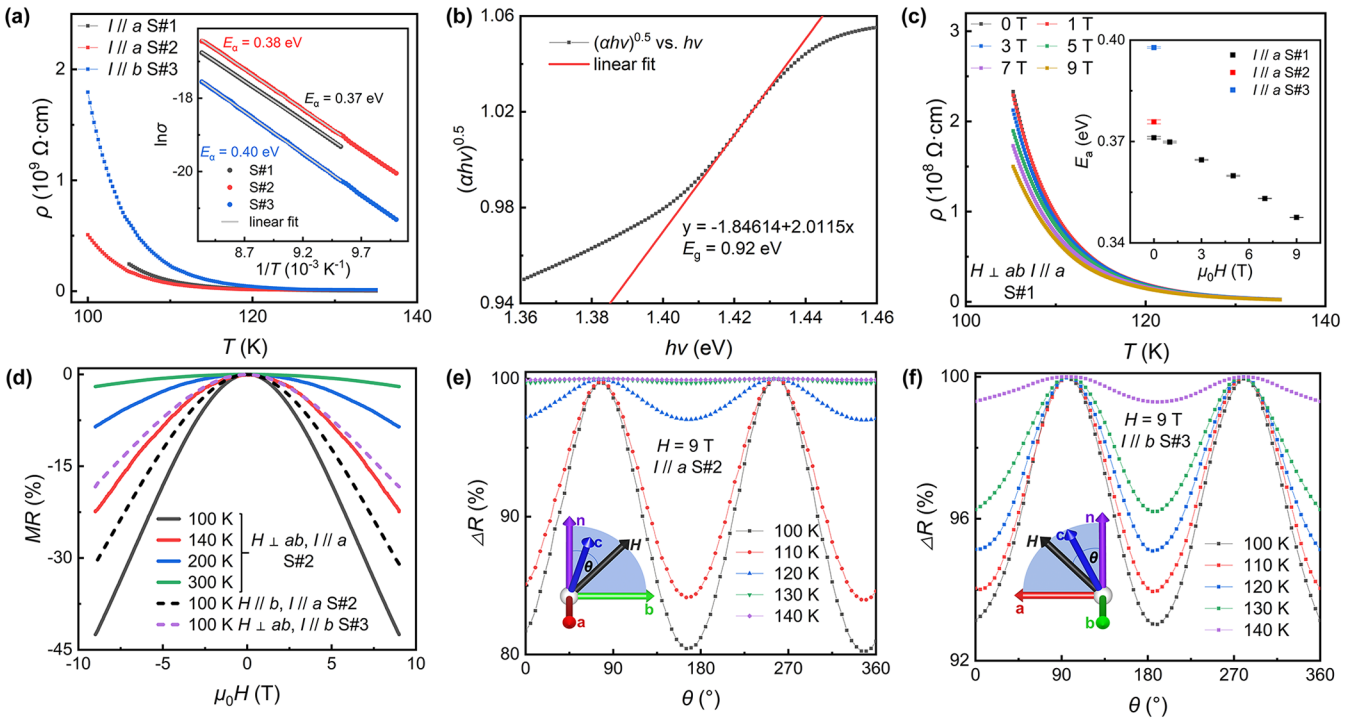


**Figure 4.** Semiconductor behavior, large NMR, and in-plane anisotropy. (a) Temperature-dependent resistivity with $I \parallel a$ (S#1 and S#2) and $I \parallel b$ (S#3). The inset shows the linear fits in the temperature range of 105−120 K based on the thermal activation model. (b) Tauc plot derived from UV−vis−IR spectra. (c) Temperature-dependent resistivity with $I \parallel a$ (S#1) under an out-of-plane ($H \perp ab$) magnetic field. The inset shows the corresponding thermal activation energy $E_\alpha$ with $I \parallel a$ and $I \parallel b$. (d) MR with $I \parallel a$ (S#2) under an out-of-plane magnetic field measured at different temperatures. The MR curves at 100 K with $I \parallel a$ under an in-plane magnetic field (dashed black line) and $I \parallel b$ (S#3) under an out-of-plane magnetic field (dashed purple line) are included for comparison. (e) Angle-dependent MR with $I \parallel a$ (S#2) and the magnetic field rotating in the plane normal to the $a$-axis. (f) Angle-dependent MR with $I \parallel b$ (S#3) and the magnetic field rotating in the plane normal to the $b$-axis. The insets in panels (e) and (f) show the magnetotransport measuring geometry, where $\theta$ denotes the angle between $H$ and the vector $n$ normal to the $ab$-plane.

$MnSi_2Te_4$ with a basal spacing of $d$ = 7.38 Å, which is consistent with $d(00l)$. The calculated interlayer distance is $d_{vdW}$ = 3.13 Å,[35] close to that of graphite and h-BN,[36,37] suggesting the vdW feature and potential applications in nanodevices when approaching the 2D limit. Through mechanical exfoliation, bulk $MnSi_2Te_4$ crystals can be easily exfoliated (Figure S5), with a thickness down to approximately 6 ± 2 nm (corresponding to ∼7 layers) as confirmed by the atomic force microscopy measurements (Figure 2f). These results indicate that $MnSi_2Te_4$ is a promising candidate for exploring low-dimensional physics and applications, given its ability to be readily exfoliated into atomically thin layers (including monolayers) through mechanical exfoliation and alternative methods.[38−40] Moreover, the unique layered structure opens up the possibility of designing a variety of DTMCs by modulating the interlayer or intralayer arrangement of established TMCs through ordered octahedral substitution.

**Magnetic Properties and Specific Heat Capacity.** The temperature-dependent magnetic susceptibility $\chi$ measured under magnetic fields with different directions is presented in Figure 3a. All magnetic susceptibility curves in zero-field-cooling (ZFC) and field-cooling (FC) protocols show a kink at $T_N$ = 18.6 K and little bifurcation below $T_N$, suggesting a possible AFM transition. $\chi_a$ and $\chi_\perp$ show only a weak temperature dependence below $T_N$, whereas $\chi_b$ drops rapidly with decreasing temperature, indicating that the easy axis is predominantly oriented along the $b$-axis. In the high-temperature paramagnetic (PM) region (150−300 K), $\chi(T)$ curves follow the Curie−Weiss law $\chi = \chi_0 + C/(T - \theta)$, where $\chi_0$ is the temperature-independent component, $C$ the Curie constant, and $\theta$ the Curie temperature. Further cooling leads to a deviation from Curie−Weiss behavior, accompanied by a broad hump of magnetic susceptibility around 40 K (∼$2T_N$), similar to the maximum of $\chi$ observed in $MnPS_3$.[41] All Curie−Weiss fittings yield negative $\theta$ with $|\theta|/T_N \approx 5 > 1$ (Figure S6a and Table S5), confirming the presence of a strong AFM interaction and moderate frustration. The fitted effective magnetic moment of Mn at high temperature, $\mu_{eff} = (8C/n)^{1/2}$ ($n$ is the number of magnetic atoms per formula), is 5.685(1) $\mu_B$/Mn for $H \parallel a$, 6.019(1) $\mu_B$/Mn for $H \parallel b$, and 6.090(2) $\mu_B$/Mn for $H \perp ab$, all close to the theoretical magnetic moment of $Mn^{2+}$ in the high-spin state ($S$ = 5/2, $\mu_{eff}$ = 5.92 $\mu_B$/Mn). These results indicate that Mn in $MnSi_2Te_4$ primarily exists as $Mn^{2+}$ ions, in agreement with the valence states derived from XPS (Figure S3). Figure 3b illustrates the anisotropic isothermal magnetization ($M(H)$), where all $M(H)$ curves exhibit typical AFM behavior at 2 K, characterized by an approximately linear field dependence and the absence of hysteresis or saturation up to 8 T. Further increasing the magnetic field results in a spin-flip transition for $H \parallel b$ with a critical field $H_{SF}$ = 10.8(8) T at 2 K, which gradually increases with increasing temperature and vanishes above $T_N$ (Figure S7).

The magnetic ground state of $MnSi_2Te_4$ was further characterized by using single-crystal neutron diffraction. As


https://doi.org/10.1021/jacs.5c13595
J. Am. Chem. Soc. 2026, 148, 340−348

revealed by the diffraction patterns at 5 K in the ($H$, 0.5, $L$) and ($H$, −0.5, $L$) planes (Figures 3c and S8), the magnetic peaks are indexed by two distinct magnetic wave vectors: $q_1$ = (0, −0.5, 0.5) and $q_2$ = (0, 0.5, −0.25). Symmetry analysis based on the magnetic wave vectors and the $P\bar{1}$ space group reveals that $MnSi_2Te_4$ exhibits a collinear G-type AFM ground state, with antiparallel aligned spins between the nearest-neighbor magnetic ions and a small tilting away from the $b$-axis in zero field (Figures 3d and S9). Compared to the crystallographic unit cell, the magnetic unit cell is doubled along both the $b$- and the $c$-axes. The magnetic moment $\boldsymbol{m}$ = (0.635(2), 1.420(4), −0.430(12)) is predominantly aligned along the $b$-axis, with a slight tilt toward the $a$- and $c$-axes.

The specific heat capacity was measured over a temperature range of 2−200 K (Figure 3e). A $\lambda$-shaped peak corresponding to the occurrence of a magnetic transition is observed at 18.8 K, in agreement with the Néel temperature determined from the magnetic susceptibility. The low-temperature specific heat capacity was fitted by the Debye model $C = \gamma T + \beta T^3$ (Figure 3f), where $\gamma T$ and $\beta T^3$ represent the electronic and phononic contributions, respectively. The Sommerfeld coefficient $\gamma$, proportional to the density of states (DOS, $g(E_F)$) at the Fermi level $E_F$, was determined to be 1.43 mJ mol$^{-1}$ K$^{-2}$ per formula unit. The near-zero DOS around $E_F$ suggests a semiconducting nature of $MnSi_2Te_4$.[42]

It should be noted that two anomalies are observed in the magnetic properties of $MnSi_2Te_4$: (i) a deviation from the Curie−Weiss law accompanied by a broad hump around 40 K in $\chi(T)$ curves, and (ii) a discrepancy between the saturated magnetic moment determined by neutron diffraction at low-temperature (1.614(8) $\mu_B$ at 5 K) and that estimated from the high-temperature Curie−Weiss fitting ($S \approx 5/2$, $\mu_{eff} \approx 5.92\ \mu_B$, $\mu_{sat} \approx 5\ \mu_B$ for $T > 150$ K). The deviation from Curie−Weiss behavior can be typically understood within two frameworks: a thermally driven spin crossover scenario,[43,44] which predominantly reduces the saturation magnetic moment and the corresponding $C$ through depopulation of the high-spin state (Figure S10), and the critical fluctuation scenario (as reported in DTMCs such as $MnPS_3$[41,45]), where the deviation from mean-field behavior enhances the critical exponent $\gamma$ in $\chi \sim (T - T_N)^{-\gamma}$ (or even crosses over to an exponential temperature dependence) due to changes in effective dimension and anisotropic exchange couplings (Table S7). In $MnSi_2Te_4$, although the $\chi_m T$ plot and the magnetic entropy derived from the specific heat capacity (Figures S6b and S11) possibly hint a partial spin crossover from the high-spin state,[43,44] the peak positions and line shapes in X-ray absorption spectroscopy (XAS) spectra did not change significantly as the temperature decreases,[46−48] only exhibiting a slight reduction in the branching ratio (Figure S12). The contributions of critical fluctuation near $T_N$ might also be an explanation, considering the quasi-2D/one-dimensional structural characteristics, leaving an interesting issue for $MnSi_2Te_4$. The comprehensive understanding will require further investigations, such as temperature-dependent XPS and Raman spectroscopy, high-field magnetization measurements, inelastic neutron scattering, and corresponding Monte Carlo simulations of the anisotropic exchange coupling.

**Electrical Transport Properties.** As shown in Figure 4a, the temperature-dependent in-plane resistivity with current applied along different directions increases monotonically with a decrease in temperature, exhibiting typical semiconductor behavior and clear in-plane anisotropy. The corresponding conductivity $\sigma_{xx} = 1/\rho_{xx}$ follows a thermally activated Arrhenius behavior $\sigma(T) = \sigma_0 e^{-\beta T}$, where $\beta = E_\alpha/2k_BT$, $k_B$ is the Boltzmann constant, $E_\alpha$ is the thermal activation energy.[49] The linear fit of ln $\sigma_{xx}$ vs $1/T$ (Figure 4a, inset) yields $E_\alpha$ = 0.37 eV with $I \parallel a$ (S#1, 0.38 eV for S#2) and 0.40 eV with $I \parallel b$ (S#3), smaller than the optical band gap ($E_g$ = 0.92 eV) determined from the Tauc plot of ultraviolet−visible−infrared (UV−vis−IR) spectra (Figure 4b).[50] Given the presence of dual-valence states in the XPS spectra (Figure S3), the discrepancy between $E_\alpha$ and $E_g$ can be attributed to the defect levels.[51]

Under an out-of-plane magnetic field (Figure 4c), the resistivity with $I \parallel a$ at the lower side of the measuring temperature decreases significantly with increasing magnetic field, and the corresponding thermal activation energy decreases monotonically. Considering the persistent substantial field dependence of magnetization at such high temperatures (Figure S7), the decrease suggests a possible magnetic-field-induced modification of the band gap, which might result in pronounced NMR.[52] Figure 4d summarizes the normalized MR $[(R(H) - R_0)/R_0 \times 100\%]$ with current applied along different directions under different magnetic fields. For $I \parallel a$, an unsaturated NMR is observed at all measured temperatures under an out-of-plane magnetic field ($H \perp ab$) up to 9 T, with the absolute value increasing monotonically with decreasing temperature and reaching −42.5% at 9 T and 100 K. By rotating the magnetic field parallel to the $b$-axis, the MR reduces to −31% at 9 T and 100 K. For $I \parallel b$, the MR only reaches −18% at 100 K under an out-of-plane magnetic field ($H \perp ab$) up to 9 T, much smaller than that for $I \parallel a$ under an out-of-plane magnetic field, further indicating the in-plane anisotropy. Angle-dependent MR reveals 2-fold symmetries with an increasing magnitude $\Delta R = [(R(\theta) - R(\theta_0))/R(\theta_0)]$ as the temperature decreases (Figure 4e,f), reaching an amplitude of ∼20% for $I \parallel a$ and ∼7% for $I \parallel b$ at 9 T and 100 K, indicating distinct anisotropic behaviors with current applied along different directions above $T_N$.

The strong resistance response to applied magnetic field is crucial for magnetic sensing and switching devices,[53] and the pronounced NMR in $MnSi_2Te_4$ is comparable to that of many established materials exhibiting large NMR at significantly lower temperatures, including $CeCuAs_2$ (−15% at 9 T, 2 K), CrSBr (−40% at 2 T, 30 K), $CrGeTe_3$ (−40% at 4 T, 65 K), and the Fe/Cr structure (−45% at 2 T, 4.2 K).[53−56] The large NMR and its relatively high occurrence temperature guarantee functional magnetic detection across a broader temperature range. The NMR persisting above the magnetic transition temperature is also observed in some TMCs with short-range ordering induced by spin fluctuations, such as $CrGeTe_3$, $CrSiTe_3$, and $CrPS_4$, where the NMR reaches the maximum near the transition temperature and sharply decreases with increasing temperature.[56−58] By contrast, the large NMR currently observed in $MnSi_2Te_4$ occurs at a temperature significantly higher than $T_N$, where the spin fluctuations are usually expected to be weak. Though there exist some AFM materials capable of sustaining NMR via strong spin fluctuations at such a high temperature, they usually exhibit magnetic structures incorporating ferromagnetic interactions (e.g., A-type AFM) and a sign reversal in the slope of resistivity at relatively high temperature, which is distinctly absent in $MnSi_2Te_4$ (G-type AFM).[59,60] Considering the persistent substantial field dependence of magnetization and the observed decrease in activation energy, the spin fluctuations


https://doi.org/10.1021/jacs.5c13595
J. Am. Chem. Soc. 2026, 148, 340−348

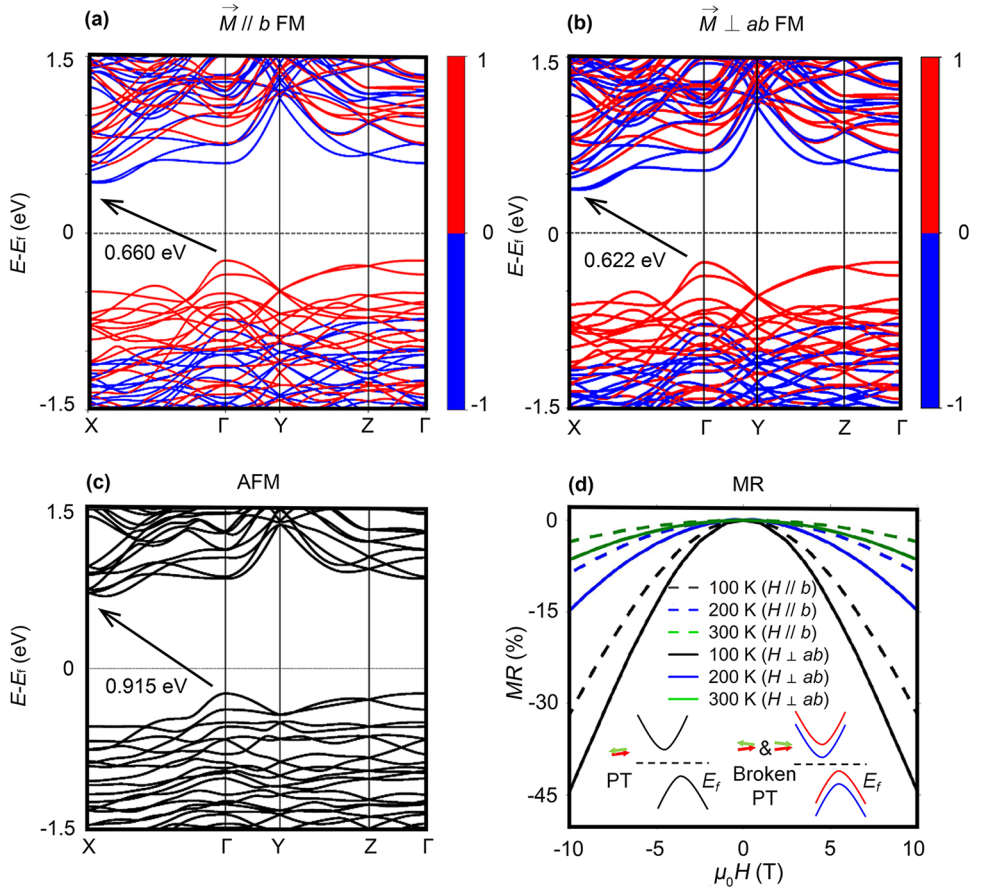


**Figure 5.** Calculated band structures and MR of $MnSi_2Te_4$. Electronic band structures of FM configurations with (a) $H \parallel b$, (b) $H \perp ab$, and (c) the AFM configuration. The corresponding spin ($\langle s \rangle$) is assigned as +1 when positive and −1 when negative. The arrows indicate the conduction band minimum and valence band maximum for each band structure. (d) Simulated MR at different temperatures. The inset demonstrates the influence of spin splitting induced by *PT* symmetry breaking on the band structure.

might be less predominant in $MnSi_2Te_4$ at such a high temperature. Nevertheless, the large NMR could be further enhanced at lower temperatures, especially in the vicinity of $T_N$, offering promising opportunities for further exploration and broadening the potential applications of $MnSi_2Te_4$ in field-sensitive devices.[9]

**Magnetic Configurations and Electronic Structure.** To understand the electrical transport properties of $MnSi_2Te_4$, the electronic band structures were investigated by using first-principles calculations with different magnetic configurations considered (Figure S14). Upon application of a sufficiently strong magnetic field along the *b*-axis or perpendicular to the *ab*-plane, $MnSi_2Te_4$ exhibits ferromagnetic (FM) configurations, with the calculated band structures demonstrating strong spin splitting, showing indirect band gaps of 0.660 and 0.622 eV (Figure 5a,b), respectively. Owing to its centrosymmetric structure, $MnSi_2Te_4$ preserves *PT* symmetry in both the AFM and PM phases, resulting in Kramers degeneracy throughout the Brillouin zone.[61] The spin-degenerate band structure of the AFM ground state in the absence of an external magnetic field (Figure 5c) was also calculated, showing an indirect band gap of 0.915 eV, which is ∼40% larger than that of the FM states. This band gap is very close to the experimentally observed ones, well above $T_N$ from the optical measurement at room temperature, validating the possibility of using the AFM band gap as that of the PM state for simplicity. The narrowing of the band gap will naturally induce an increase in conductivity, resulting in the observed NMR under an external magnetic field. As depicted in Figure 5a,b, the narrowing of the band gap would happen as the external magnetic field begins to polarize the randomly oriented magnetic moments in the PM state. During the polarization, *PT* symmetry breaking induces spin splitting of bands, lifting the Kramers degeneracy, thereby reducing the band gap and subsequently triggering NMR. According to the experimentally measured isothermal magnetization curves, the anisotropic large NMR can be accurately described by the Drude model (Figure 5d, see Note S5 for details), demonstrating the validity of the spin splitting mechanism as the origin of the observed large NMR.

## CONCLUSIONS

In summary, we have synthesized a new vdW AFM semiconductor $MnSi_2Te_4$. $MnSi_2Te_4$ belongs to the family of DTMCs but demonstrates a distinctive in-plane architecture featuring a heterostructure with a zigzag arrangement of distorted [$MnTe_6$] and [$Si_2Te_6$] octahedra. Magnetic susceptibility, isothermal magnetization, and single-crystal neutron diffraction measurements reveal collinear G-type AFM ordering, with the easy axis oriented approximately along the *b*-axis and a Néel temperature $T_N$ = 18.6 K. The temperature-dependent resistivity and MR exhibit typical semiconductor behavior, with pronounced unsaturated NMR at temperatures significantly above $T_N$. The electronic structure, determined through first-principles calculations, explains the observed


https://doi.org/10.1021/jacs.5c13595
J. Am. Chem. Soc. 2026, 148, 340−348

NMR via spin splitting induced by *PT* symmetry breaking, which aligns with the magnetic and electrical transport properties. These results indicate that $MnSi_2Te_4$ not only demonstrates the feasibility of designing DTMCs with unique octahedral arrangements and properties through intralayer structural modulation but also serves as a promising candidate for investigating low-dimensional magnetism and developing field-sensitive devices and next-generation spintronic devices.

## ■ ASSOCIATED CONTENT

### Supporting Information

The Supporting Information is available free of charge at https://pubs.acs.org/doi/10.1021/jacs.5c13595.

Details of experimental and computational methods, crystallographic data, EDS, XPS, and XAS spectra, HAADF-STEM images and SAED patterns, optical images of flakes, Curie−Weiss fitting, magnetic entropy, isothermal magnetization, single-crystal neutron diffraction patterns, calculated magnetic anisotropic energy, and band structures of $MnSi_2Te_4$ (PDF)

### Accession Codes

Deposition Number 2454477 contains the supplementary crystallographic data for this paper. These data can be obtained free of charge via the joint Cambridge Crystallographic Data Centre (CCDC) and Fachinformationszentrum Karlsruhe Access Structures service.

## ■ AUTHOR INFORMATION


### Corresponding Authors

**Long Chen** − *Department of Physics and Astronomy, University of Tennessee, Knoxville, Tennessee 37996, United States;* orcid.org/0000-0003-1992-8434; Email: lchen64@utk.edu

**Quansheng Wu** − *Beijing National Laboratory for Condensed Matter Physics, Institute of Physics, Chinese Academy of Sciences, Beijing 100190, China; University of Chinese Academy of Sciences, Beijing 100049, China;* orcid.org/0000-0002-9154-4489; Email: quansheng.wu@iphy.ac.cn

**Gang Wang** − *Beijing National Laboratory for Condensed Matter Physics, Institute of Physics, Chinese Academy of Sciences, Beijing 100190, China;* orcid.org/0000-0001-9110-3942; Email: gangwang@iphy.ac.cn

### Authors

**Ke Liao** − *Beijing National Laboratory for Condensed Matter Physics, Institute of Physics, Chinese Academy of Sciences, Beijing 100190, China; University of Chinese Academy of Sciences, Beijing 100049, China*

**Bo Yin** − *Beijing National Laboratory for Condensed Matter Physics, Institute of Physics, Chinese Academy of Sciences, Beijing 100190, China; University of Chinese Academy of Sciences, Beijing 100049, China*

**Yue Pan** − *Beijing National Laboratory for Condensed Matter Physics, Institute of Physics, Chinese Academy of Sciences, Beijing 100190, China; University of Chinese Academy of Sciences, Beijing 100049, China*

**Chen Liu** − *Beijing Synchrotron Radiation Facility, Institute of High Energy Physics, Chinese Academy of Sciences, Beijing 100049, China*

**Yan Wu** − *Neutron Scattering Division, Oak Ridge National Laboratory, Oak Ridge, Tennessee 37831, United States*

**Seung-Hwan Do** − *Materials Science and Engineering Department, University of Tennessee, Knoxville, Tennessee 37996, United States*

**Yifan Gao** − *Department of Physics, Hong Kong University of Science and Technology, Clear Water Bay, Hong Kong, China*

**Yaling Yang** − *Beijing National Laboratory for Condensed Matter Physics, Institute of Physics, Chinese Academy of Sciences, Beijing 100190, China; University of Chinese Academy of Sciences, Beijing 100049, China*

**Yulong Wang** − *Beijing National Laboratory for Condensed Matter Physics, Institute of Physics, Chinese Academy of Sciences, Beijing 100190, China; University of Chinese Academy of Sciences, Beijing 100049, China*

**Xuhui Wang** − *Beijing National Laboratory for Condensed Matter Physics, Institute of Physics, Chinese Academy of Sciences, Beijing 100190, China; University of Chinese Academy of Sciences, Beijing 100049, China*

**Ying Li** − *Beijing National Laboratory for Condensed Matter Physics, Institute of Physics, Chinese Academy of Sciences, Beijing 100190, China*

**Zhongnan Guo** − *Department of Chemistry, School of Chemistry and Biological Engineering, University of Science and Technology Beijing, Beijing 100083, China;* orcid.org/0000-0003-4907-4679

**Junwei Liu** − *Department of Physics, Hong Kong University of Science and Technology, Clear Water Bay, Hong Kong, China;* orcid.org/0000-0001-8051-7349

**Jiaou Wang** − *Beijing Synchrotron Radiation Facility, Institute of High Energy Physics, Chinese Academy of Sciences, Beijing 100049, China*

**Dong Su** − *Beijing National Laboratory for Condensed Matter Physics, Institute of Physics, Chinese Academy of Sciences, Beijing 100190, China; University of Chinese Academy of Sciences, Beijing 100049, China;* orcid.org/0000-0002-1921-6683

**Jie Ma** − *School of Physics and Astronomy, Shanghai Jiao Tong University, Shanghai 200240, China;* orcid.org/0000-0002-7060-1325

Complete contact information is available at: https://pubs.acs.org/10.1021/jacs.5c13595

### Author Contributions

[¶]K.L., B.Y., and Y.P contributed equally to this work.


### Notes

This article has been authored by UT-Battelle, LLC under Contract DEAC05-00OR22725 with the U.S. Department of Energy. The United States Government retains and the publisher, by accepting the article for publication, acknowledges that the United States Government retains a nonexclusive, paid-up, irrevocable, worldwide license to publish or reproduce the published form of this manuscript, or allow others to do so, for United States Government purposes. The Department of Energy will provide public access to these results of federally sponsored research in accordance with the DOE Public Access Plan (http://energy.gov/downloads/doe-public-access-plan). Attempts to synthesize DTMCs with a similar structure resulted in a layered nonmagnetic semiconductor $MgSi_2Te_4$, which features a similar intralayer zigzag arrangement but a different stacking order, suggesting the potential for further extending the DTMC family with a zigzag intralayer arrangement.

The authors declare no competing financial interest.

## ■ ACKNOWLEDGMENTS

K.L. and G.W. would like to thank Prof. X. L. Chen of the Institute of Physics, Chinese Academy of Sciences, for fruitful discussions. B.Y. and Q.W. would like to thank Z. H. Liu and Z. Y. Song of the Institute of Physics, Chinese Academy of Sciences, for fruitful discussions. This work was partially supported by the National Natural Science Foundation of China (Grant Nos. 52325201 and 11888101), the National Key Research and Development Program of China (Grant Nos. 2023YFA1607400 and 2022YFA1403900), and the sample preselection and characterization station of the Synergetic Extreme Condition User Facility. We thank the staff from the BL07U beamline of the Shanghai Synchrotron Radiation Facility for their assistance with XAS data collection. The neutron part of this research used resources at the High Flux Isotope Reactor, a DOE Office of Science User Facility operated by the Oak Ridge National Laboratory. The beam time was allocated to the WAND$^2$ instrument on proposal number IPTS-33282.1.

## ■ REFERENCES

(1) Zou, X.; Xu, Y.; Duan, W. 2D materials: rising star for future applications. *Innovation* **2021**, *2*, No. 100115.
(2) Wang, P.; Ge, J.; Li, J.; Liu, Y.; Xu, Y.; Wang, J. Intrinsic magnetic topological insulators. *Innovation* **2021**, *2*, No. 100098.
(3) Matsukura, F.; Tokura, Y.; Ohno, H. Control of magnetism by electric fields. *Nat. Nanotechnol.* **2015**, *10*, 209−220.
(4) Gibertini, M.; Koperski, M.; Morpurgo, A. F.; Novoselov, K. S. Magnetic 2D materials and heterostructures. *Nat. Nanotechnol.* **2019**, *14*, 408−419.
(5) Awschalom, D. D.; Flatté, M. E. Challenges for semiconductor spintronics. *Nat. Phys.* **2007**, *3*, 153−159.
(6) Li, X.; Wu, X.; Li, Z.; Yang, J.; Hou, J. Bipolar magnetic semiconductors: a new class of spintronics materials. *Nanoscale* **2012**, *4*, 5680−5685.
(7) Mi, M.; Xiao, H.; Yu, L.; Zhang, Y.; Wang, Y.; Cao, Q.; Wang, Y. Two-dimensional magnetic materials for spintronic devices. *Mater. Today Nano* **2023**, *24*, No. 100408.
(8) Zhong, D.; Seyler, K. L.; Linpeng, X.; Cheng, R.; Sivadas, N.; Huang, B.; Schmidgall, E.; Taniguchi, T.; Watanabe, K.; McGuire, M. A.; et al. Van der Waals engineering of ferromagnetic semiconductor heterostructures for spin and valleytronics. *Sci. Adv.* **2017**, *3*, No. e1603113.
(9) Lenz, J.; Edelstein, S. Magnetic sensors and their applications. *IEEE Sens. J.* **2006**, *6*, 631−649.
(10) Manzeli, S.; Ovchinnikov, D.; Pasquier, D.; Yazyev, O. V.; Kis, A. 2D transition metal dichalcogenides. *Nat. Rev. Mater.* **2017**, *2*, No. 17033.
(11) Yu, Y.; Nam, G. H.; He, Q.; Wu, X.; Zhang, K.; Yang, Z.; Chen, J.; Ma, Q.; Zhao, M.; Liu, Z.; et al. High phase-purity 1T′-$MoS_2$-and 1T′-$MoSe_2$-layered crystals. *Nat. Chem.* **2018**, *10*, 638−643.
(12) Ye, J.; Liao, K.; Ge, X.; Wang, Z.; Wang, Y.; Peng, M.; He, T.; Wu, P.; Wang, H.; Chen, Y.; et al. Narrowing Bandgap of $HfS_2$ by Te Substitution for Short-Wavelength Infrared Photodetection. *Adv. Opt. Mater.* **2021**, *9*, No. 2002248.
(13) Luo, H.; Xie, W.; Tao, J.; Inoue, H.; Gyenis, A.; Krizan, J. W.; Yazdani, A.; Zhu, Y.; Cava, R. J. Polytypism, polymorphism, and superconductivity in $TaSe_{2-x}Te_x$. *Proc. Natl. Acad. Sci. U.S.A.* **2015**, *112*, E1174−E1180.
(14) Fan, X.; Chen, H.; Deng, J.; Sun, X.; Zhao, L.; Chen, L.; Jin, S.; Wang, G.; Chen, X. Effects of Rb intercalation on $NbSe_2$: phase formation, structure, and physical properties. *Inorg. Chem.* **2019**, *58*, 7564−7570.
(15) Yu, Y.; Yang, F.; Lu, X. F.; Yan, Y. J.; Cho, Y.; Ma, L.; Niu, X.; Kim, S.; Son, Y.; Feng, D.; et al. Gate-tunable phase transitions in thin flakes of 1T-$TaS_2$. *Nat. Nanotechnol.* **2015**, *10*, 270−276.
(16) Shu, Z.; Wang, H.; Jo, N. H.; Jozwiak, C.; Bostwick, A.; Rotenberg, E.; Xie, W.; Kong, T. Synthesis and physical properties of a new layered ferromagnet $Cr_{1.21}Te_2$. *Phys. Rev. Mater.* **2023**, *7*, No. 044406.
(17) Fuh, H. R.; Chang, C. R.; Wang, Y. K.; Evans, R. F.; Chantrell, R. W.; Jeng, H. T. Newtype single-layer magnetic semiconductor in transition-metal dichalcogenides $VX_2$ (X = S, Se and Te). *Sci. Rep.* **2016**, *6*, No. 32625.
(18) Zhang, J.; Yang, B.; Zheng, H.; Han, X.; Yan, Y. Large magnetic anisotropy and strain induced enhancement of magnetic anisotropy in monolayer $TaTe_2$. *Phys. Chem. Chem. Phys.* **2017**, *19*, 24341−24347.
(19) Guo, H.; Lu, N.; Wang, L.; Wu, X.; Zeng, X. C. Tuning electronic and magnetic properties of early transition-metal dichalcogenides via tensile strain. *J. Phys. Chem. C* **2014**, *118*, 7242−7249.
(20) Li, J.; Zhao, B.; Chen, P.; Wu, R.; Li, B.; Xia, Q.; Guo, G.; Luo, J.; Zang, K.; Zhang, Z.; et al. Synthesis of ultrathin metallic $MTe_2$ (M = V, Nb, Ta) single-crystalline nanoplates. *Adv. Mater.* **2018**, *30*, No. 1801043.
(21) Sun, X.; Li, W.; Wang, X.; Sui, Q.; Zhang, T.; Wang, Z.; Liu, L.; Li, D.; Feng, S.; Zhong, S.; et al. Room temperature ferromagnetism in ultra-thin van der Waals crystals of 1T-$CrTe_2$. *Nano Res.* **2020**, *13*, 3358−3363.
(22) Jiang, X.; Liu, Q.; Xing, J.; Liu, N.; Guo, Y.; Liu, Z.; Zhao, J. Recent progress on 2D magnets: Fundamental mechanism, structural design and modification. *Appl. Phys. Rev.* **2021**, *8*, No. 031305, DOI: 10.1063/5.0039979.
(23) Li, X.; Cao, T.; Niu, Q.; Shi, J.; Feng, J. Coupling the valley degree of freedom to antiferromagnetic order. *Proc. Natl. Acad. Sci. U.S.A.* **2013**, *110*, 3738−3742.
(24) Ni, Z.; Haglund, A.; Wang, H.; Xu, B.; Bernhard, C.; Mandrus, D.; Qian, X.; Mele, E.; Kane, C.; Wu, L. Imaging the Néel vector switching in the monolayer antiferromagnet $MnPSe_3$ with strain-controlled Ising order. *Nat. Nanotechnol.* **2021**, *16*, 782−787.
(25) Ostwal, V.; Shen, T.; Appenzeller, J. Efficient spin-orbit torque switching of the semiconducting van der Waals ferromagnet $Cr_2Ge_2Te_6$. *Adv. Mater.* **2020**, *32*, No. 1906021.
(26) Gong, C.; Li, L.; Li, Z.; Ji, H.; Stern, A.; Xia, Y.; Cao, T.; Bao, W.; Wang, C.; Wang, Y.; et al. Discovery of intrinsic ferromagnetism in two-dimensional van der Waals crystals. *Nature* **2017**, *546*, 265−269.
(27) Zhu, W.; Song, C.; Han, L.; Guo, T.; Bai, H.; Pan, F. Van der Waals lattice-induced colossal magnetoresistance in $Cr_2Ge_2Te_6$ thin flakes. *Nat. Commun.* **2022**, *13*, No. 6428.
(28) Zhang, C.; Wang, L.; Gu, Y.; Zhang, X.; Xia, X.; Jiang, S.; Huang, L.; Fu, Y.; Liu, C.; Lin, J.; et al. Hard ferromagnetic behavior in atomically thin $CrSiTe_3$ flakes. *Nanoscale* **2022**, *14*, 5851−5858.
(29) Li, Z.; Bai, W.; Li, Y.; Li, Y.; Wang, S.; Zhang, W.; Zhao, J.; Sun, Z.; Xiao, C.; Xie, Y. Coexistence of large positive and negative magnetoresistance in $Cr_2Si_2Te_6$ ferromagnetic semiconductor. *Sci. China Mater.* **2022**, *65*, 780−787.
(30) Seo, J.; De, C.; Ha, H.; Lee, J. E.; Park, S.; Park, J.; Skourski, Y.; Choi, E. S.; Kim, B.; Cho, G. Y.; et al. Colossal angular magnetoresistance in ferrimagnetic nodal-line semiconductors. *Nature* **2021**, *599*, 576−581.
(31) Zhang, Y.; Ni, Y.; Zhao, H.; Hakani, S.; Ye, F.; DeLong, L.; Kimchi, I.; Cao, G. Control of chiral orbital currents in a colossal magnetoresistance material. *Nature* **2022**, *611*, 467−472.
(32) Carteaux, V.; Brunet, D.; Ouvrard, G.; Andre, G. Crystallographic, magnetic and electronic structures of a new layered ferromagnetic compound $Cr_2Ge_2Te_6$. *J. Phys.: Condens. Matter* **1995**, *7*, 69.
(33) Ouvrard, G.; Sandre, E.; Brec, R. Synthesis and crystal structure of a new layered phase: The chromium hexatellurosilicate $Cr_2Si_2Te_6$. *J. Solid State Chem.* **1988**, *73*, 27−32.
(34) Chittari, B. L.; Park, Y.; Lee, D.; Han, M.; MacDonald, A. H.; Hwang, E.; Jung, J. Electronic and magnetic properties of single-layer $MPX_3$ metal phosphorous trichalcogenides. *Phys. Rev. B* **2016**, *94*, No. 184428.

(35) Liu, Y.; Huang, Y.; Duan, X. Van der Waals integration before and beyond two-dimensional materials. *Nature* **2019**, *567*, 323−333.
(36) Bernal, J. D. The structure of graphite. *Proc. R. Soc. London, Ser. A* **1924**, *106*, 749−773.
(37) Pease, R. S. An X-ray study of boron nitride. *Acta Crystallogr.* **1952**, *5*, 356−361.
(38) Wang, Q. H.; Kalantar-Zadeh, K.; Kis, A.; Coleman, J. N.; Strano, M. S. Electronics and optoelectronics of two-dimensional transition metal dichalcogenides. *Nat. Nanotechnol.* **2012**, *7*, 699−712.
(39) Niu, L.; Coleman, J. N.; Zhang, H.; Shin, H.; Chhowalla, M.; Zheng, Z. Production of two-dimensional nanomaterials via liquid-based direct exfoliation. *Small* **2016**, *12*, 272−293.
(40) Huang, Y.; Pan, Y.; Yang, R.; Bao, L.; Meng, L.; Luo, H.; Cai, Y.; Liu, G.; Zhao, W.; Zhou, Z.; et al. Universal mechanical exfoliation of large-area 2D crystals. *Nat. Commun.* **2020**, *11*, No. 2453.
(41) Long, G.; Zhang, T.; Cai, X.; Hu, J.; Cho, C.; Xu, S.; Shen, J.; Wu, Z.; Han, T.; Lin, J.; et al. Isolation and characterization of few-layer manganese thiophosphite. *ACS Nano* **2017**, *11*, 11330−11336.
(42) Li, B.-Z.; Wu, S.; Xiang, J.; Zhu, Q.; Liu, Y.; Cao, C.; Cao, G. Antiferromagnetic insulating state in quasi-one-dimensional $K_2Cr_3As_3H$. *Sci. China: Phys., Mech. Astron.* **2023**, *66*, No. 237411.
(43) Gavara-Edo, M.; Córdoba, R.; Valverde-Muñoz, F. J.; Herrero-Martín, J.; Real, J. A.; Coronado, E. Electrical sensing of the thermal and light-induced spin transition in robust contactless spin-crossover/graphene hybrid devices. *Adv. Mater.* **2022**, *34*, No. 2202551.
(44) Ksenofontov, V.; Gaspar, A. B.; Gütlich, P. Pressure Effect Studies on Spin Crossover and Valence Tautomeric Systems. *Spin Crossover in Transition Metal Compounds III*; Springer: Berlin, Heidelberg, 2004; pp 23−64.
(45) Wildes, A.; Rønnow, H. M.; Roessli, B.; Harris, M.; Godfrey, K. Static and dynamic critical properties of the quasi-two-dimensional antiferromagnet $MnPS_3$. *Phys. Rev. B* **2006**, *74*, No. 094422.
(46) Thole, B. T.; Van der Laan, G. Branching ratio in x-ray absorption spectroscopy. *Phys. Rev. B* **1988**, *38*, 3158.
(47) Cramer, S. P.; DeGroot, F.; Ma, Y.; Chen, C.; Sette, F.; Kipke, C.; Eichhorn, D.; Chan, M.; Armstrong, W.; Libby, E.; et al. Ligand field strengths and oxidation states from manganese L-edge spectroscopy. *J. Am. Chem. Soc.* **1991**, *113*, 7937−7940.
(48) Miyamachi, T.; Gruber, M.; Davesne, V.; Bowen, M.; Boukari, S.; Joly, L.; Scheurer, F.; Rogez, G.; Yamada, T. K.; Ohresser, P.; et al. Robust spin crossover and memristance across a single molecule. *Nat. Commun.* **2012**, *3*, No. 938.
(49) Tauc, J. *Amorphous and Liquid Semiconductors*; Springer: New York, 2012.
(50) Bai, Y.; Yang, P.; Wang, P.; Xie, H.; Dang, H.; Ye, L. Semimetal bismuth mediated UV−vis-IR driven photo-thermocatalysis of $Bi_4O_5I_2$ for carbon dioxide to chemical energy. *J. $CO_2$ Util.* **2018**, *23*, 51−60.
(51) Nkum, R.; Adimado, A.; Totoe, H. Band gap energies of semiconducting sulphides and selenides. *Mater. Sci. Eng., B* **1998**, *55*, 102−108.
(52) Zhang, S.; Fang, Z.; Weng, H.; Wu, Q. The inadequacy of the $\rho$-$T$ curve for phase transitions in the presence of magnetic fields. *Innovation* **2025**, *6*, No. 100837.
(53) Baibich, M. N.; Broto, J. M.; Fert, A.; Van Dau, F. N.; Petroff, F.; Etienne, P.; Creuzet, G.; Friederich, A.; Chazelas, J. Giant magnetoresistance of (001) Fe/(001) Cr magnetic superlattices. *Phys. Rev. Lett.* **1988**, *61*, 2472.
(54) Chen, L.; Gu, Y.; Wang, Y.; Zhou, Y.; Liao, K.; Pan, Y.; Wu, X.; Li, Y.; Wang, Z.; Ma, Y. Large negative magnetoresistance beyond chiral anomaly in topological insulator candidate $CeCuAs_2$ with spin-glass-like behavior. *Innovation Mater.* **2023**, *10*, No. 100011, DOI: 10.59717/j.xinn-mater.2023.100011.
(55) Telford, E. J.; Dismukes, A. H.; Lee, K.; Cheng, M.; Wieteska, A.; Bartholomew, A. K.; Chen, Y. S.; Xu, X.; Pasupathy, A. N.; Zhu, X.; et al. Layered antiferromagnetism induces large negative magnetoresistance in the van der Waals semiconductor CrSBr. *Adv. Mater.* **2020**, *32*, No. 2003240.
(56) Zhuo, W.; Lei, B.; Wu, S.; Yu, F.; Zhu, C.; Cui, J.; Sun, Z.; Ma, D.; Shi, M.; Wang, H.; et al. Manipulating ferromagnetism in few-layered $Cr_2Ge_2Te_6$. *Adv. Mater.* **2021**, *33*, No. 2008586.
(57) Li, Y.; Chen, Z.; Wang, J.; li, T.; Tian, M.; Karel, J.; Suzuki, K. Abnormal thickness-dependent magneto-transport properties of vdW magnetic semiconductor $Cr_2Si_2Te_6$. *npj 2D Mater. Appl.* **2023**, *7*, No. 39.
(58) Wu, F.; Gibertini, M.; Watanabe, K.; Taniguchi, T.; Gutiérrez-Lezama, I.; Ubrig, N.; Morpurgo, A. F. Gate-controlled magnetotransport and electrostatic modulation of magnetism in 2D magnetic semiconductor $CrPS_4$. *Adv. Mater.* **2023**, *35*, No. 2211653.
(59) Blawat, J.; Marshall, M.; Singleton, J.; Feng, E.; Cao, H.; Xie, W.; Jin, R. Unusual electrical and magnetic properties in layered $EuZn_2As_2$. *Adv. Quantum Technol.* **2022**, *5*, No. 2200012.
(60) Ma, J.-Z.; Nie, S.; Yi, C.; Jandke, J.; Shang, T.; Yao, M.; Naamneh, M.; Yan, L.; Sun, Y.; Chikina, A.; et al. Spin fluctuation induced Weyl semimetal state in the paramagnetic phase of $EuCd_2As_2$. *Sci. Adv.* **2019**, *5*, No. eaaw4718.
(61) Zhao, Y.; Chen, C.; Sheng, X.; Yang, S. A. Switching spinless and spinful topological phases with projective $PT$ symmetry. *Phys. Rev. Lett.* **2021**, *126*, No. 196402.